

SCALE DEPENDENT FLOW DIRECTIONS OF RIVERS

SUBMITTED, NON-PEER REVIEWED MANUSCRIPT, COMPILED OCTOBER 19, 2020

Alex G. Lipp¹* and Gareth G. Roberts¹

¹Department of Earth Sciences and Engineering, Imperial College London, UK

ABSTRACT

Large rivers play crucial roles in determining locations of civilisation, biodiversity and nutrient supply to the oceans. The paths that rivers take across the Earth's surface vary considerably with scale. For example, at large scales big rivers have simple flow paths that can be described by a few changes in direction. However, at smaller scales, in headwaters or meanders for example, their paths can change rapidly. We map the scales at which river planforms are set so that their positions can be objectively compared to driving processes at appropriate scales (e.g. crust and lithospheric thicknesses, lithology, mantle convection, biota). To do so, we develop a spectral methodology to map flow directions as a function of distance and scale (wavenumber). The results show that flow directions of the Colorado river in Western North America is set at large scales, $O(10^3)$ km, which we tentatively suggest is a consequence of sub-plate support.

PLAIN LANGUAGE SUMMARY

The location of rivers controls the development of civilization, biodiversity and the supply of material to the oceans. However, determining the specific location of rivers on the Earth's surface remains a challenge. On small scales, rivers change direction rapidly, forming structures such as meanders. However, over longer distances, their shape is often more simple, flowing away from regions of mountain building. We develop a method that quantitatively describes the shape of rivers over different distances. We can use this to remove the small scale variations in flow directions (e.g. meanders) to better reveal the more significant large scale component. This method is demonstrated using the Colorado river in the USA. We demonstrate that the large scale component of flow-direction runs parallel to the line-of-descent of Earth's gravity field. This result is consistent with Western North American topography being controlled by mantle convection.

1 INTRODUCTION

Despite its general importance, the way in which drainage networks acquire their planforms is poorly understood across different length scales. Evolution of the solid Earth is an obvious means to determine flow paths via lithospheric motions driven by, for example, orogenesis, crustal thickening and mantle convection. Geologic, hydraulic, sedimentological and biotic processes also control flow paths. Antecedence, hysteresis, complex erosional processes and human intervention are also important means by which drainage networks can be generated and modified (Cox 1989; Rinaldo et al. 1993; Anderson and Anderson 2010). The processes controlling drainage planforms are, to some degree, scale dependent. This contribution is concerned with splitting the flow direction of rivers into constituent scales and identifying where the dominant signals are generated.

In many instances visual inspection of drainage planforms provides most of the information we need. For example, the Colorado river, which drains western North America, flows mostly to the west, southwest and south in its upper, mid- and lower reaches, respectively (Figure 1). The planform of rivers atop topographic swells in other continents also have similarly simple patterns at long, $O(10^3-10^4)$ km, wavelengths (Rudge et al. 2015). At these long wavelengths rivers mostly flow away from crests of topographic swells that are supported by the mantle (Roberts et al. 2012; Braun et al. 2013; Faccenna et al. 2019). This pattern of emergent simplicity at long wavelengths is manifest in the flow paths of many large rivers draining topographic swells and tectonic topography on Earth, e.g. African swells, Colorado Plateau, Mexican Highlands, East Australian High-

lands, Himalayas, and elsewhere, e.g. Tharsis Rise, Mars (Black et al. 2017). However, most rivers clearly do not have simple flow paths at all lengths scales. At short (< 100 km) length scales they can be extremely variable, which sometimes results in rivers flowing in the opposite direction to the long wavelength direction of flow (e.g. Goosenecks, San Juan river, North America). These simple observations indicate that river planforms are scale dependent. To formalise these observations we develop a spectral methodology to map planforms and flow directions as a function of scale and position. We explore one way in which this approach can be used to compare drainage patterns to environmental variables at appropriate scales.

River flow directions do not obviously change in a periodic manner. Therefore, standard Fourier spectral analysis is not well suited for our purposes. Instead we make use of continuous wavelet transforms (Daubechies 1990; Farge 1992; Kumar and Foufoula-Georgiou 1997; Torrence and Compo 1998). There is a precedent for transforming directional time series into the frequency and frequency-distance domains in the atmospheric and oceanic sciences and a spherical harmonic approach has been used to compare flow directions of rivers to long wavelength topography (Donelan et al. 1985, 1996; Black et al. 2017). Recent wavelet spectral analyses of longitudinal river profiles, i.e. elevation as a function of distance, $z(x)$, has shown that the shape of large African rivers is mostly determined at wavelengths > 100 km where their power spectra, $\phi(k)$, can be characterised as red noise, i.e. $\phi \propto k^{-2}$, where k is wavenumber (Roberts et al. 2019). At shorter wavelengths power appears to have a pink noise spectrum, $\phi \propto k^{-1}$. These observations give a basis for

*correspondence: a.lipp18@imperial.ac.uk,

gareth.roberts@imperial.ac.uk

modelling longitudinal river profiles as systems that possess self-similar scaling and deterministic behaviour at long wavelengths that emerges through local complexity. It gives a basis for understanding why at large length scales, $O(10^2-10^3)$ km, river profiles atop dynamically supported topography (e.g. Bié dome, West Africa) have common shapes (Roberts 2019). In this study, we develop wavelet spectral techniques to map flow directions of continental-scale drainage patterns as a function of distance and wavelength.

2 DATA AND METHODS

This section contains, first, a description of data used to extract drainage patterns and second, methodologies to perform wavelet transformations of a series of directions. Software to perform directional wavelet analysis is provided (github.com/alexlipp/directional-wavelets).

Transforming a series of directions (in the form of an azimuth between 0 and 360°) has several simple steps. First, the drainage dataset is extracted from the ASTER GDEM, which has a horizontal resolution of ~ 30 m, using Esri’s D8 (steepest descent) flow routing algorithms. Second, latitudes and longitudes are resampled along flow paths (e.g. rivers) so that they have equidistant spacing, which makes them straightforward to transform into the spectral domain. In the examples used in this paper $\delta x = 2$ km. Third, distances and azimuths are calculated along the path. Local (point-to-point) azimuths, $\theta(x)$, are extracted using the `gmt mapproject` algorithm (see digital repository). Note that input is expected to be positions along a river with longitudes and latitudes in decimal degrees and resolution of up to a few tens of meters.

Applying wavelet transforms to a series of azimuths is challenging because the functions are discontinuous—at least one pole contains a discontinuity, e.g. $\sin(360) = \sin(0)$. To avoid this issue we transform the complex form of azimuthal series, $a(x)$. Azimuths can be considered as complex numbers of unit magnitude and variable phase, θ . Making use of Euler’s formula any azimuth, θ , can be represented as $\exp(i\theta)$ with real part $\cos(\theta)$ and imaginary part $\sin(\theta)$, which correspond to northings and eastings, respectively. The complex series to be transformed is

$$a(x) = \exp\left[\frac{i\theta\pi}{180}\right], \quad (1)$$

where θ varies between 0 and 360° . The azimuth series was normalised to zero mean, e.g. $a'(x) = a(x) - \bar{a}$, prior to transformation. The resultant series of complex numbers was transformed to generate

$$W_x^{a'}(s) = \sum_{a'=0}^{N-1} a'(x)\psi\left[\frac{x'-x}{s}\right]. \quad (2)$$

The mother wavelet ψ is scaled by s and translated along the series by x' for N data points. In the examples shown in this paper the mother wavelet is a real valued 6th order derivative of a Gaussian (DOG), with $\delta_j = 0.1$ (Torrence and Compo 1998). $W_x^{a'}(s)$ is the transformed version of the complex azimuth series as a function of scale, s . Power of the complex series is $|W_x^{a'} + \bar{a}|^2$. Scales are converted to Fourier periods (Torrence and Compo 1998).

Real valued azimuths (in degrees) as a function of distance and wavenumber can then be calculated as $\theta(x, k) = \zeta 180/\pi \bmod 360$, where \bmod is the modulus operator, and ζ is the argument of the transformed (complex) series (Equation 2). ζ is computed as

$$\zeta = \tan^{-1}\left[\frac{\Im\{W_x^{a'}(\theta, k) + \bar{a}\}}{\Re\{W_x^{a'}(\theta, k) + \bar{a}\}}\right]. \quad (3)$$

Note that the mean of the complex series, \bar{a} , is added to the reconstructed complex series in this step. The inverse wavelet transformation is simply the sum of the signal in distance-wavenumber space over scales, $j = 0, 1, \dots, J$. The inverse transformation of the complex series is

$$a_x = \bar{a} + \frac{\delta_j \delta t^{1/2}}{1.7379} \sum_{j=0}^J \frac{W_x^{a'}(s_j)}{s_j^{1/2}}, \quad (4)$$

for the DOG mother wavelet used in this study (Torrence and Compo 1998). Note that the subscript x denotes a transformed series. The denominator factor (here 1.7379) depends on the mother wavelet used in the transformation. Real valued azimuths (in degrees) can be generated from a_x

$$\theta_x = \tan^{-1}\left[\frac{\Im\{a_x\}}{\Re\{a_x\}}\right] \frac{180}{\pi} \bmod 360. \quad (5)$$

Filtered azimuth series can now be generated by solving Equations (4) and (5) between the scales of interest. Filtered river planforms can be estimated from these azimuths by forward geodetic transformation, which returns longitudes and latitudes given a starting position (e.g. the head of the river), azimuths and distances. In this case, distances are scaled so that the final calculated position coincides with the actual river mouth. The WGS84 datum was used to perform the transformation. Whilst we consider only river paths in this study, it is straightforward to generalise this approach to other sequential paths or directional data (e.g. a time series of flow velocities and directions).

An alternative more intuitive methodology is to transform eastings and northings generated from the azimuthal series. As expected, this approach gives the same results as transforming the complex form of the signal (Figure 1c-g of this document). Eastings and northings are calculated such that

$$e(x) = \sin(\pi\theta(x)/180), \quad n(x) = \cos(\pi\theta(x)/180), \quad (6)$$

where $e(x)$ and $n(x)$ vary between -1 and 1 , θ is in degrees. The easting and northing distance-amplitude series are then independently transformed into the distance-wavenumber domain. The series were normalised to zero mean, e.g. $e'(x) = e(x) - \bar{e}$, prior to transformation. These real valued series are converted using a continuous wavelet transformation and real valued mother wavelets. The two series, $e'(x)$ or $n'(x)$, are transformed such that

$$W_x^e(s) = \sum_{x'=0}^{N-1} e'_x \psi\left[\frac{x'-x}{s}\right], \quad W_x^n(s) = \sum_{x'=0}^{N-1} n'_x \psi\left[\frac{x'-x}{s}\right], \quad (7)$$

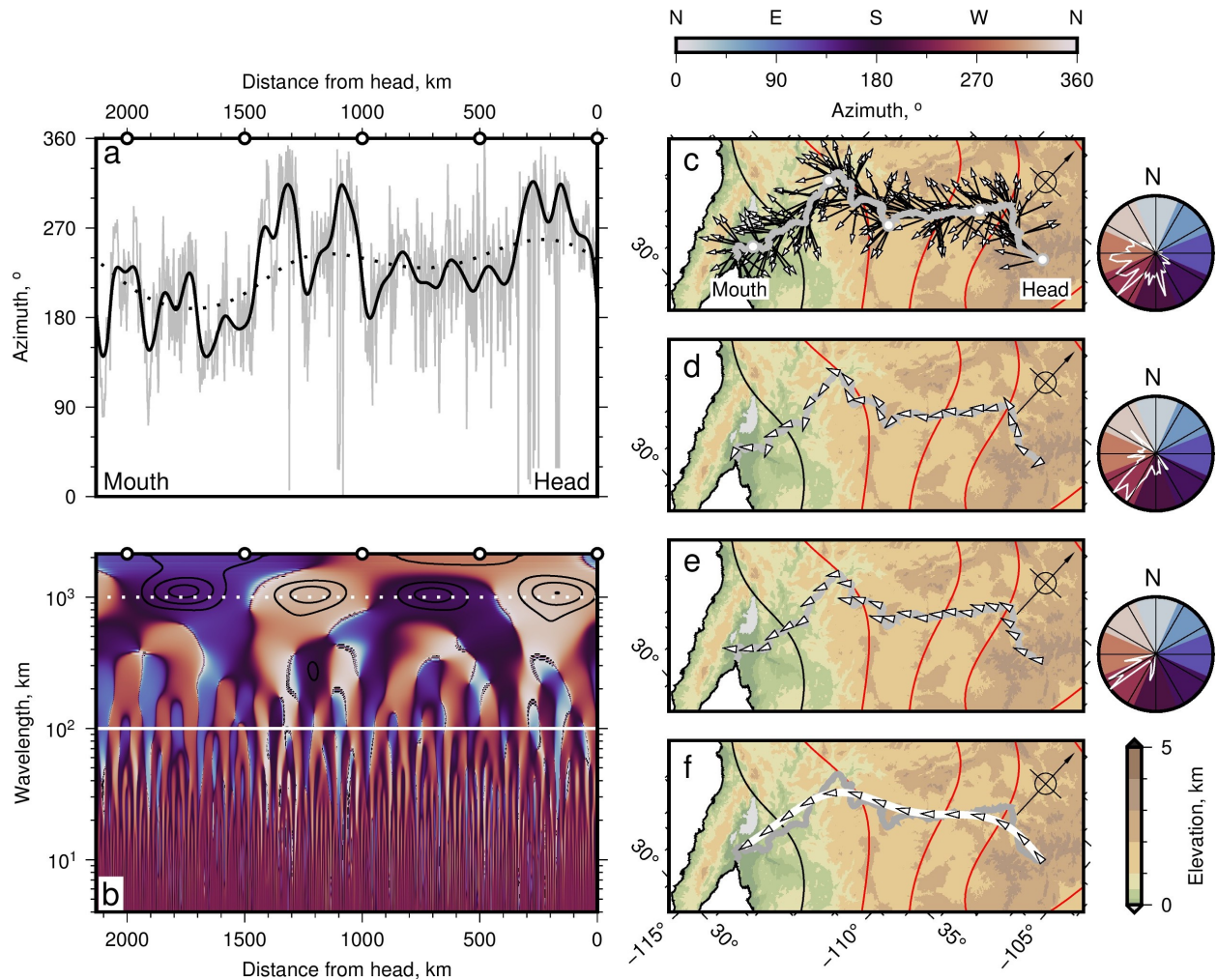


Figure 1: Deconvolution of flow directions: Example from Colorado river. (a) Gray curve = calculated azimuths of Colorado river ($\delta x = 2$ km). Solid and dotted black curves = azimuths filtered to remove wavelengths $\lambda < 100$ km and < 1000 km, respectively. Note that distance is from river head and azimuths are measured in downstream direction. (b) Azimuths as function of distance and wavelength. Colours are centred on cardinals and intercardinals; light blue/dark blue/purple/orange = north/east/south/west; see scale bar and rose diagrams aside panels c–e. Solid and dotted white lines = 1000 km and 100 km wavelengths, respectively. Black contours = regions with highest power. White circles atop panel = positions along river (see panel c). (c) Colorado river (gray) and flow directions (azimuths) of full resolution dataset ($\delta x = 2$ km); directions are shown every ~ 10 km for clarity. White circles = distances shown atop panels (a) and (b). Colours/contours = topography/long wavelength (> 800 km) free-air gravity anomalies, contour interval = 10 mGal, red/black contours = positive/zero values. Inset compass rose points north. Rose diagram aside shows azimuths of full resolution dataset ($\delta x = 2$ km) in 5° bins (white polygon); rose sectors are coloured by azimuth (see panel b). (d) & (e) White vectors = azimuths calculated using wavelengths $\lambda > 100$ km and > 1000 km, respectively. Gray = Colorado river. Rose diagrams aside show calculated azimuths for filtered datasets in 5° bins. (f) White curve = river planform from geodetic transform of long wavelength azimuths. Vectors = long wavelength (> 1000 km) flow azimuths shown every ~ 150 km for clarity.

where $W_x^e(s)$ and $W_x^n(s)$ are the transformed versions of the easting and northing series as a function of scale, s . The easting and northing distance-amplitude series can be reconstructed by summing their respective wavelet transforms across scales (i.e. the inverse transformation). Following Torrence and Compo's notation,

$$e_x = \frac{\delta_j \delta t^{1/2}}{1.7379} \sum_{j=0}^J \frac{W_x^e(s_j)}{s_j^{1/2}}, \quad \text{and} \quad n_x = \frac{\delta_j \delta t^{1/2}}{1.7379} \sum_{j=0}^J \frac{W_x^n(s_j)}{s_j^{1/2}}, \quad (8)$$

for the DOG mother wavelet used in this study. At this stage the means (e.g. \bar{e} and \bar{n}) are added to the reconstructed series. The azimuth series as a function of distance can then be constructed using

$$\theta_x = \frac{180}{\pi} \arctan2(e_x + \bar{e}, n_x + \bar{n}). \quad (9)$$

Filtering of the azimuth series is performed by solving Equation (8) between scales of interest and calculating θ_x using filtered eastings and northings (Equation 9).

There are two main sources of uncertainty in the wavelet transformation described above. First, there is uncertainty in the position of mapped river planforms. The fidelity of mapped rivers was assessed by comparison with independent satellite imagery. At the scales of interest (i.e. > 2 km) planforms are accurately reproduced away from flat topography and standing water (e.g. lakes). There is also an uncertainty, $\delta\theta$ associated with measuring azimuths from discrete digital elevation data, which is inversely proportional to distance between cells, L , such that $\sin(\delta\theta) = \delta x (\delta x^2 + L^2)^{-1/2}$ for simple east-west Euclidean flow paths, which yields an uncertainty of $\delta\theta \sim 0.9^\circ$ for ASTER data ($\delta x \approx 30$ m) if $L = 2$ km. If $L = 100$ km, $\delta\theta \sim 0.02^\circ$. Second, spectral leakage can generate uncertainties in calculated azimuths. A guide to the fidelity of the wavelet transform is the accuracy of reconstituted series (i.e. generated by inverse transformation), which, for the examples in this paper, match the $\theta(x)$ series within a few percent in terms of error of the mean.

3 RESULTS

We tested this approach by transforming flow directions of the Colorado river, which flows across the Colorado Plateau, through the Grand Canyon, to the Gulf of California (Figure 1).

Figure 1 shows the results of transforming the flow direction of the Colorado river into distance-wavenumber space. Figure 1a shows measured azimuths from an evenly resampled ($\delta x = 2$ km) dataset alongside the filtered series for wavelengths > 100 km and > 1000 km. Figure 1b shows Colorado river azimuths as a function of distance and wavelength ($1/k$). In Figure 1c the azimuths for the full resolution dataset are shown as vectors with the observed river superimposed on top. These vectors are spread broadly uniformly between $150^\circ \leq \theta \leq 300^\circ$ (see rose diagram aside Figure 1c). Note that the map has been rotated. The filtered > 100 km and > 1000 km azimuths and their associated rose diagrams are shown in Figures 1d and 1e. These long wavelength flow directions have, as expected,

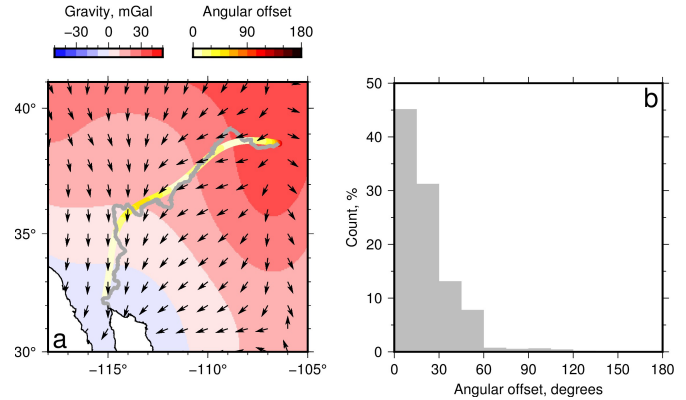


Figure 2: Comparison of observed long wavelength flow directions of the Colorado river and predicted sub-plate support. (a) Red-white-blue color scale = long wavelength free-air gravity anomalies (~ 800 – 2500 km) from GRACE dataset, which are a rough guide to loci of sub-plate support (Tapley et al. 2005; Colli et al. 2016). Vectors = flow directions (gradients) calculated using gravity data, i.e. g' . Colored curve = position of river calculated by forward geodetic transformation of long wavelength (> 1000 km) component of azimuths; colors = angular offset between azimuths of long wavelength components of actual river and g' (see Figure 1f; color interval = 15°). (b) Histogram (binwidth = 15°) showing difference (angular offset) between azimuths calculated from gravity data and long wavelength flow paths.

a smaller spread than the full dataset. The long wavelength azimuthal series ($\lambda > 1000$ km) quantifies flow paths mapped by eye in the introductory section, i.e. flow to west ($\sim 270^\circ$), southwest ($\sim 240^\circ$) and south ($\sim 190^\circ$) in the upper, mid and lower reaches of the river, respectively (Figure 1f).

The white curve in Figure 1f shows a pseudo-Colorado river path generated using only azimuths at wavelengths > 1000 km and forward geodetic transformation. This calculated flow path reinforces our assertion that most of the long wavelength structure of the Colorado river is set by just two changes in flow direction.

Gravity anomalies, tomographic models, magmatism and isostatic calculations (which include crustal thickness estimates) indicate that western North American topography is principally a consequence of sub-crustal support moderated by tectonic and erosional processes (Atwater 1970; Wernicke 1985; Fernandes et al. 2019). A guide to the amplitude and wavelength of sub-plate support is the transfer function (admittance) between long wavelength free-air gravity and topography (McKenzie 2010). We note that gravity anomalies at spherical harmonic degrees appropriate for this study, $O(1000)$ km, are particularly sensitive to upper mantle structure (Colli et al. 2016). In western North America the calculated admittance is $\sim 25 \pm 3$ mGal/km at wavelengths > 1000 km, which implies that up to ~ 1.5 km of western North American topography is supported by the mantle (Stephenson et al. 2014). Figure 1c–f shows long wavelength free-air gravity from the GRACE dataset filtered to extract wavelengths between ~ 800 – 2500 km Tapley et al. 2005.

By removing the short wavelength (< 1000 km) contributions to flow directions, we can now compare the planform of the

Colorado river to putative sub-plate support at appropriate scales. We investigate the role the mantle plays in maintaining flow directions by comparing flows paths to gravity data. We start by assuming that long wavelength free-air gravity anomalies are a proxy for sub-plate support. Under the hypothesis of mantle supported topography, the long-wavelength flow-direction of the Colorado river should flow parallel to the line of steepest gravity descent. The direction of steepest descent is calculated from the first derivative of the gravity field, $\arctan2(g'_x, g'_y)$, where g'_x and g'_y are the first derivatives of the gravity field in x and y directions. Figure 2a demonstrates that the long wavelength components of the Colorado river are parallel/sub-parallel to the direction of g' along its length. $> 75\%$ of the offsets between the Colorado river and g' are $< 30^\circ$ in magnitude (Figure 2b). We tentatively suggest that these results indicate the importance of sub-plate support in setting the planform of the Colorado river.

4 CONCLUSIONS

In this study a continuous wavelet approach is used to transform the complex form of distance-azimuth series into the distance-wavenumber domain. The position of the Colorado river is principally controlled by the shape of long wavelength $O(10^2 - 10^3)$ km topography. We tentatively suggest that the correlation between long wavelength gravity anomalies and river flow directions indicates the importance of sub-plate support in maintaining the flow direction of the Colorado river at these scales. We suggest comparing mapped spectral power of azimuthal series to other environmental variables could give insight into shape and origin of planforms at all scales.

CODE AVAILABILITY

Software to perform the directional wavelet analysis is provided at: github.com/alexlipp/directional-wavelets. ASTER Topographic data can be accessed at from asterweb.jpl.nasa.gov/gdem.asp. Wavelet transforms were performed using a modified version of the python mply library (Albanese et al. 2012).

ACKNOWLEDGEMENTS

We thank V.Fernandes and F. Richards for helpful discussion. AGL is funded by the Natural Environment Research Council Grantham Institute SSCP DTP (grant number NE/L002515/1). This work was supported by CASP and the Leverhulme Trust (grant number RPG-2019-073).

REFERENCES

Albanese, D., R. Visintainer, S. Merler, S. Riccadonna, G. Jurman, and C. Furlanello (2012). *mlpy: Machine Learning Python*. arXiv: 1202.6548 [cs].
 Anderson, R. S. and S. P. Anderson (2010). *Geomorphology: The Mechanics and Chemistry of Landscapes*. 1st ed. Cambridge, UK: Cambridge University Press.
 Atwater, T. (1970). “Implications of Plate Tectonics for the Cenozoic Tectonic Evolution of Western North America”. *Geological Society of America Bulletin* 81, pp. 3513–3536.

Black, B. A., J. T. Perron, D. Hemingway, E. Bailey, F. Nimmo, and H. Zebker (2017). “Global drainage patterns and the origins of topographic relief on Earth, Mars, and Titan”. *Science* 356.6339, pp. 727–731. doi: 10.1126/science.aag0171.
 Braun, J., X. Robert, and T. Simon-Labric (2013). “Eroding dynamic topography”. *Geophysical Research Letters* 40.8, pp. 1494–1499. doi: 10.1002/grl.50310.
 Colli, L., S. Ghelichkhanand, and H.-P. Bunge (2016). “On the ratio of dynamic topography and gravity anomalies in a dynamic Earth”. *Geophysical Research Letters* 43, pp. 2510–2516. doi: 10.1002/2016GL067929.
 Cox, K. G. (1989). “The role of mantle plumes in the development of continental drainage patterns”. *Nature* 342, pp. 873–877.
 Daubechies, I. (1990). “The wavelet transform, time-frequency localization and signal analysis”. *IEEE Transactions on Information Theory* 36.5, pp. 961–1005. doi: 10.1109/18.57199.
 Donelan, M. A., W. M. Drennan, and A. K. Magnusson (1996). “Nonstationary Analysis of the Directional Properties of Propagating Waves”. *Journal of Physical Oceanography* 26.9, pp. 1901–1914. doi: 10.1175/1520-0485(1996)026<1901:NAOTDP>2.0.CO;2.
 Donelan, M. A., J. Hamilton, and W. H. Hui (1985). “Directional spectra of wind-generated ocean waves”. *Philosophical Transactions of the Royal Society of London. Series A, Mathematical and Physical Sciences* 315, pp. 509–562. doi: 10.1098/rsta.1985.0054.
 Faccenna, C., P. Glisovic, A. Forte, T. W. Becker, E. Garzanti, A. Sernbroni, and Z. Gvirtzman (2019). “Role of dynamic topography in sustaining the Nile River over 30 million years”. *Nature Geoscience*. doi: 10.1038/s41561-019-0472-x.
 Farge, M. (1992). “Wavelet transforms and their applications to turbulence”. *Annual Review of Fluid Mechanics* 24.1, pp. 395–458. doi: 10.1146/annurev.fl.24.010192.002143.
 Fernandes, V. M., G. G. Roberts, N. White, and A. C. Whittaker (2019). “Continental-Scale Landscape Evolution: A History of North American Topography”. *Journal of Geophysical Research: Earth Surface* 124. doi: 10.1029/2018JF004979.
 Kumar, P. and E. Foufoula-Georgiou (1997). “Wavelet analysis for geophysical applications”. *Reviews of Geophysics* 35.4, pp. 385–412. doi: 10.1029/97RG00427.
 McKenzie, D. (2010). “The influence of dynamically supported topography on estimates of T_e ”. *Earth and Planetary Science Letters* 295, pp. 127–138.
 Rinaldo, A., I. Rodriguez-Iturbe, R. Rigon, E. Ijjasz-Vasquez, and R. L. Bras (1993). “Self-organized fractal river networks”. *Phys. Rev. Lett.* 70 (6), pp. 822–825. doi: 10.1103/PhysRevLett.70.822.
 Roberts, G. G. (2019). “Scales of Similarity and Disparity Between Drainage Networks”. *Geophysical Research Letters* 46.7, pp. 3781–3790. doi: 10.1029/2019GL082446.
 Roberts, G. G., N. J. White, G. L. Martin-Brandis, and A. G. Crosby (2012). “An uplift history of the Colorado Plateau and its surroundings from inverse modeling of longitudinal river profiles”. *Tectonics* 31.4. doi: 10.1029/2012TC003107.
 Roberts, G. G., N. White, and B. H. Lodhia (2019). “The generation and scaling of longitudinal river profiles”. *Journal of Geophysical Research: Earth Surface* 124, pp. 137–153. doi: 10.1029/2018JF004796.
 Rudge, J. F., G. G. Roberts, N. J. White, and C. N. Richardson (2015). “Uplift histories of Africa and Australia from

- linear inverse modeling of drainage inventories”. *Journal of Geophysical Research. Earth Surface* 120, pp. 894–914. doi: [10.1002/2014JF003297](https://doi.org/10.1002/2014JF003297).
- Stephenson, S. N., G. G. Roberts, M. J. Hoggard, and A. C. Whittaker (2014). “A Cenozoic uplift history of Mexico and its surroundings from longitudinal river profiles”. *Geochemistry, Geophysics, Geosystems* 15, pp. 4734–4758. doi: [10.1002/2014GC005425](https://doi.org/10.1002/2014GC005425).
- Tapley, B., J. Ries, S. Bettadpur, D. Chambers, M. Cheng, F. Condi, B. Gunter, Z. Kang, P. Nagel, R. Pastor, T. Pekker, S. Poole, and F. Wang (2005). “GGM02 — An improved Earth gravity field model from GRACE”. *J. Geodesy* 79.467. doi: [10.1007/s00190-005-0480-z](https://doi.org/10.1007/s00190-005-0480-z).
- Torrence, C. and G. P. Compo (1998). “A Practical Guide to Wavelet Analysis”. *Bulletin of the American Meteorological Society* 79, pp. 61–78.
- Wernicke, B. (1985). “Uniform-sense normal simple shear of the continental lithosphere”. *Canadian Journal of Earth Sciences* 22.1, pp. 108–125. doi: [10.1139/e85-009](https://doi.org/10.1139/e85-009).